Scientific Reports

https://doi.org/10.1038/s41598-025-32415-x

Article in Press

Electric-field-enhanced high performance of monolayer polyaniline g-C_3N for lung cancer identification: a DFT study

Received: 18 September 2025

Accepted: 10 December 2025

Published online: 19 December 2025

Cite this article as: Omidvari M.H., Safaiee R., Sheikhi M.H. *et al.* Electric-field-enhanced high performance of monolayer polyaniline g-C_3N for lung cancer identification: a DFT study. *Sci Rep* (2025). https://doi.org/10.1038/s41598-025-32415-x

M. H. Omidvari, R. Safaiee, M. H. Sheikhi & Sh. Nasresfahani

Electric-field-enhanced high performance of monolayer polyaniline g-C_3N for lung cancer identification: A DFT study

M. H. Omidvari [a], R. Safaiee [b,*], M. H. Sheikhi [a], Sh. Nasresfahani [c]

[a] School of Electrical and Computer Engineering, Shiraz University, Shiraz, Iran

[b] Faculty of Advanced Technologies, Shiraz University, Shiraz, Iran

[c] Electrical and Computer Engineering Group, Golpayegan College of Engineering, Isfahan University of Technology, Golpayegan 87717-67498, Iran

***Corresponding Author:** (R. Safaiee) Safaiee@shirazu.ac.ir

Abstract

Early cancer diagnosis relies heavily on finding appropriate materials to recognize relevant biomarkers. In this study, we conduct a first-principle density functional theory simulation to investigate the capability of two-dimensional polyaniline (g-C_3N) for detecting propane and acetaldehyde, as known lung cancer biomarkers. The energetically most favorable configurations of the adsorbed systems were determined, and the computed adsorption energy reveals the non-covalent interaction between biomarkers and g-C_3N monolayer. As a result, the adsorption process is reversible, which is fundamental for the long lifespan of biosensors in real applications. On the other hand, acetaldehyde physisorption on the g-C_3N monolayer induces a significant variation in the band gap, suggesting the possible use of g-C_3N as a resistance-based biosensor. Charge transfer analysis shows that both biomarkers act as electron acceptors from the host material. The capability of the g-C_3N monolayer to respond to these biomarkers was also investigated upon applying an external electric field. An electric field considerably enhances the interaction between gas molecules and the g-C_3N monolayer by increasing the adsorption energies and charge transfer values, which are more pronounced for acetaldehyde. The results also show that the g-C_3N monolayer energy band gap in the presence of biomarkers closes at high electric fields. These findings highlight the ability to adjust the sensing properties of the g-C_3N monolayer through an external electric field without requiring any structural modifications.

Keywords: g-C_3N monolayer, Lung cancer biomarkers, Density functional theory, Electric field.

1. Introduction

With the rapid increase in environmental pollutants as well as the worldwide prevalence of smoking, the incidence of lung cancer, with the most cancer-related morbidity and mortality cases, has grown in adult men and women [1-4]. Conventional diagnostic techniques such as computed tomography (CT), chest X-rays, sputum cytology, bold proteomic patterns, nuclear magnetic resonance (NMR), and lung biopsies can only provide a definite diagnosis at an advanced stage of the cancer [5]. Therefore, the survival rate of patients with this cancer type is low. However, early diagnosis and efficient therapy for this cancer hold paramount significance in increasing the chance of treatment success before it spreads in the human body [6]. Recently, pinpoint identification of lung cancer biomarkers using biosensors has emerged as a viable alternative to the frequently used, costly, time-consuming, and invasive diagnostic techniques [7]. These biomarkers may be present in body fluids such as blood, serum, urine, plasma, or even within the exhaled breath of a cancerous patient [7,8]. Among them, exhaled human breath, which contains more than 200 volatile organic compounds (VOCs) in trace concentrations, is the most available diagnostic sample since it is released intuitively and in large quantities. These VOCs with exogenous or endogenous origin belong to various categories of ketones, alcohols, aldehydes, alkanes, nitriles, and benzene [8-10]. Clinical trial reports showed that changes in the composition and concentrations of VOCs correlate with variations in the health status of various body compartments [9-11]. Hence, recognizing the specific VOCs in expiratory air provides an opportunity to discern the potential patients. The most common VOCs, such as benzene, toluene, acetone, and isoprene, are frequently used in the screening of lung cancer due to their high repeatability. However, their presence is also associated with other pathologies, such as kidney stones and bronchitis [9]. Within this context, acetaldehyde (CH_3CHO) and propane (C_3H_8) are considered to be the most exclusively detected biomarkers that specifically appear in lung cancer patients' exhalations breath [9,11-13]. Empirical evidence confirms that acetaldehyde production is tumor-dependent, correlating with tumor size and ceasing upon malignant cell elimination, thereby providing a more specific diagnostic signal [14]. From this perspective, the search for materials with desirable reactivity to exploit in the field of respiratory diagnostics would be a priority.

In the last decade, the scientific community's attention has turned to graphene-like two-dimensional (2D) materials as efficient materials for detecting various toxic gases and biomolecules [15-21]. They are excellent choices for developing nanoplatforms featuring extraordinary functionalities for both cancer diagnosis and therapeutics. One of the derivatives of graphene, 2D polyaniline (g-C_3N), was first proposed theoretically and then successfully synthesized through various routes [22]. Its primitive cell consists of six C atoms and two N atoms arranged in a graphene-like honeycomb lattice structure with a homogeneous distribution of nitrogen atoms. Strong covalent interactions between C-C and C-N bonds contribute to the exceptional stability of g-C_3N [23]. In addition, its distinctive physicochemical attributes, like high thermal stability at high temperatures, high electron and hole mobilities, high specific surface area with favorable accessibility, and finite energy band gap coupled with tunable magnetic and electronic properties, satisfy the important requirements for biosensing applications [24-28]. Moreover, substituting C atoms by N atoms breaks the chemical inertness of graphene and reduces its work function, leading to better chemical activity of g-C_3N towards gas molecules [29]. Since this is a newly synthesized material, theoretical calculations are expected to guide future experimental observations. In this regard, several theoretical studies were conducted based on density functional theory (DFT) to explore the adsorption of specific targets on the g-C_3N monolayer [25, 30-34]. Drawing on earlier studies, in this work, we propose a biosensor based on two-dimensional polyaniline with the capability of detecting propane and acetaldehyde associated with the development of lung cancer. A comparative analysis of the structural and electronic properties of the g-C_3N monolayer in the presence of acetaldehyde and propane molecules is provided using DFT. On the other hand, the interaction between the g-C_3N monolayer and lung cancer biomarkers has also been considered in the presence of a vertical electric field ranging from 0.03 V/Å to 0.22 V/Å. To the best of our knowledge, it is the first time that the sensitivity of the pristine g-C_3N monolayer to these biomarkers has been studied. It was disclosed that the g-C_3N monolayer has a high affinity toward the acetaldehyde molecule thanks to dipole-dipole interactions. Furthermore, the external electric field appreciably impacts the adsorption and electronic behavior of the g-C_3N monolayer. It is anticipated that the findings of this study serve as a theoretical basis for guiding related experimental research.

We organized the rest of the paper as follows: The detailed methodology we used in this simulation is presented in Section 2. A comparison between the calculated geometric and

electronic properties of pristine g-C_3N with the corresponding data reported in the literature is given in this section to validate the method. The geometry, adsorption, and desorption behavior, and the corresponding electronic properties of the g-C_3N monolayer in the presence of lung cancer biomarkers, as well as an external electric field, are discussed in detail in Section 3. Lastly, we outline the main results in Section 4.

2. Computational details and validation

All theoretical calculations related to the gas detection functionality of the g-C_3N monolayer were accomplished on the basis of Kohn-Sham spin-polarized density functional theory, as implemented in the celebrated Quantum-ESPRESSO simulation package [35]. To deal with the electron exchange-correlation energies, the generalized gradient approximation (GGA) in the parameterization scheme of Perdew−Burke−Ernzerhof (PBE) was considered [36,37]. The ion-electron potential was replaced by an ultrasoft pseudopotential in the Rappe Rabe Kaxiras Joannopoulos scheme. Grimme's DFT-D2 semiempirical dispersion correction method with default values was taken into consideration to better understand the long-range van der Waals (vdW) interactions [38]. The optimum cutoff energy value (60 Ry) for the plane wave expansion is visually identifiable in **Figure S1(a)** as the minimum value at which the absolute change in the total energy of the system falls below the predefined tolerance. The optimal cutoff energy of 600 Ry was chosen for the charge density.

The hexagonal structure of the g-C_3N monolayer in the X-Y plane was created by expanding the optimized unit cell to a 2 × 2 supercell; each supercell consists of 24 carbon atoms and 8 nitrogen atoms. A large vacuum region of 20 Å was introduced along the conventional *z* direction to eliminate the possible interaction between g-C_3N monolayers in neighboring supercells (**Figure S1(b)**). The summation over the Brillouin zone was carried out with a k-point sampling according to the Γ-centered Monkhorst-Pack scheme with a K-space grid of 9×9×1 for geometry optimization (**Figure S1(c)**), while a denser K-space grid of 18×18×1 was chosen to calculate the electronic properties. All of these parameters were carefully chosen after several calculations to obtain well-converged results. Gaussian smearing with a standard deviation of 0.01 Ry was adopted to guarantee accuracy. The standard Broyden-Fletcher-Goldfarb-Shanno (BFGS) algorithm was used for all structural relaxations without restrictions on the movement of atoms until the maximum Hellmann-Feynman force acting on each atom was less than 1×10^{-3} Ry/a_0

(where a_0 is the Bohr radius). The self-consistent field convergence criterion was set to 1×10^{-4} Ry.

The electric field along the *z* direction was simulated by a sawtooth-like potential with a period equal to the unit cell length to study its effect on the structural and adsorption properties of the g-C_3N monolayer [39]. Its strength ranged from 0.03 to 0.22 V/Å, which lies within the experimentally achievable range for 2D systems [40, 41].

For the sake of benchmarking the adopted calculation method, the structural and electronic properties of the g-C_3N monolayer were calculated using the method described above and compared with those reported previously in the literature. The optimized structure of the pristine g-C_3N monolayer is illustrated in **Figure 1(a)**. We can see that the supercell of the pristine g-C_3N is comprised of two kinds of hexagonal rings: those composed of both C and N atoms, or those composed of only C atoms. The average bond lengths of C-C and C-N in the planar structure of g-C_3N were calculated to be 1.410 Å and 1.411 Å, respectively, which is in good agreement with earlier theoretical studies [26,29]. The optimized lattice constant of 4.887 Å was obtained by fitting the total energy versus lattice parameter with Murnaghan's equation of state [42].

The spin-distinct electronic band structure and the total density of states calculation results, accompanied by the projected density of states (PDOS) of the relaxed g-C_3N monolayer, are illustrated in **Figure 1(b)**. The Fermi energy level was set to zero and depicted by a thin horizontal red dashed line. Notably, the electronic band structure of the g-C_3N primitive cell exhibits an indirect band gap of 0.437 eV, with the valence band maximum at the M point and the conduction band minimum at the Γ point (**Figure S2**), in accordance with the literature [25,33]. However, in repeated primitive cells, the valence band maximum moved to the Γ-point according to the band folding theory [24]. Therefore, the g-C_3N monolayer is a direct semiconductor with the valence and conduction bands lying 0.2218 eV below and 0.2153 eV above the Fermi energy level, respectively. A lower energy band gap stands for higher electrical conductivity, reactivity, and sensitivity. The symmetry of the computed energy band structures and the DOS for spin-up and spin-down confirms the nonmagnetic nature of the g-C_3N monolayer. The computed PDOS uncovers that the major contribution to the valence band comes from the hybridization of the p_z orbitals of C and N atoms, while the conduction band is mainly contributed by p_z orbitals of C atoms.

Figure 2 shows the corresponding charge density distribution plot of the g-C_3N monolayer. The probability of the presence of spin-down and spin-up electrons is shown by the magenta and olive clouds in parts (a) and (b), respectively. What is vividly clear from parts (a) and (b) of this figure is the accumulation of negative charges around the nitrogen atoms, originating from the comparable electronegativity difference between C and N. On account of the non-magnetic nature of the g-C_3N monolayer, the population of spin-up and spin-down electrons around the nitrogen atoms is identical. The total charge density, which is equal to the sum of the spin-up and spin-down charge densities, as well as the spin-distinct charge density created by the difference between the spin-up and spin-down charge densities, is depicted in **Figures 2(c)** and **(d)**. The total charge density distribution is shown in amber color. The flaxen (purple) clouds in the spin-distinct charge density plot represent the excess of spin-up (spin-down) electrons around nitrogen (carbon). According to the obtained results, the g-C_3N monolayer sensing features can be predicted effectively and accurately using the described procedure.

3. Adsorption performance of pristine g-C_3N monolayer

In the next subsections, we explore the possibility of using the pristine g-C_3N monolayer as a gas-sensing material for two typical lung cancer biomarkers. To this end, the adsorption attributes of biomarkers on the g-C_3N monolayer are conversed based on structural properties conjugated with electronic ones. In addition, the impact of external electric field strength on the interaction of the host material with the gas molecules is investigated, enabling the control of adsorption attributes.

To get the most energetically favorable adsorption configuration of two lung cancer biomarkers on the g-C_3N monolayer, six highly symmetric sites were taken into account: the top sites located above the C and N atoms (TC and TN), the bridge sites positioned above the midpoint of the C-C and C-N bonds ($TM_{(CC)}$ and $TM_{(CN)}$), and the hollow sites situated on the center of the hexagonal pure carbon ring and nitrogenated carbon ring ($TH_{(CC)}$ and $TH_{(CN)}$). For each site, configurations with different gas molecule orientations were examined. Regarding acetaldehyde, four initial molecular orientations with respect to the g-C_3N surface were considered (**Figure S3**). In the first and second orientations, the acetaldehyde molecular plane was located parallel to the substrate plane, while in the other two orientations, the molecular plane was located perpendicular to the substrate. The O atom pointed either to the substrate or away from it. Taking propane, three

different orientations were considered for the possible adsorption sites (**Figure S4**). The initial adsorption distance between the related molecules and the adsorbed surface was set to 3 Å**.** **Figures 3 and 4** exhibit all possible adsorption configurations of each biomarker on the g-C_3N monolayer. Geometric optimization of all configurations was conducted by varying the atomic positions across all three dimensions, and the corresponding adsorption energy (E_{ads}) was calculated according to equation (1) [43]:

$$E_{ads} = E_{complex} - (E_{substrate} + E_{bimarker}), \quad (1)$$

where $E_{complex}$ refers to the total energy of the fully relaxed structure of g-C_3N in the presence of adsorbate, the sum of energies, $E_{substrate} + E_{bimarker}$, stands for the total energy of the pristine g-C_3N monolayer (substrate) and the isolated bimarker. The negative value of the adsorption energy represents an exothermic adsorption process, while the positive adsorption energy value implies that the adsorption is an endothermic process. The adsorption distance was defined as the distance between the g-C_3N surface and the nearest atom of the biomarker molecule. Notably, the adsorption configuration with the lowest E_{ads} is the most thermodynamically stable one and is considered for further analysis.

Based on calculated $E_{ads,}$ the recovery time for each biomarker was calculated on the basis of the van't-Hoff-Arrhenius expression [43]:

$$\tau = \nu^{-1} \exp\ (-E_{ads} / k_B T) \quad (2)$$

where ν, k_B, and T represent the attempt frequency, the Boltzmann constant (8.617×10^{-5} eV K^{-1}), and the temperature.

The adsorption process can be accompanied by charge transfer. The Löwdin charge analysis method was considered to calculate the charge transfer value (Q) between the biomarker and substrate. A negative Q suggests the electron-donating property of the adsorbed biomarker, while a positive Q signifies the electron-accepting property of the adsorbed biomarker. Furthermore, the chemical or physical interaction can be ascribed to the amount of charge transfer [43].

The direction of charge transfer between the adsorbed molecule and the substrate material was also determined by the work function(W). The work function is defined as the minimum amount of energy required to remove an electron from the Fermi level into the vacuum and is calculated as follows [44]:

$$W = V_{vac} - E_F \quad (3)$$

where E_F is the Fermi energy of the corresponding material and V_{vac} is the electrostatic potential energy of the electron at a distance from the material's surface.

The charge-density redistribution at the adsorption site, owing to charge transfer between each biomarker and the g-C_3N monolayer, was further studied by the following equation [44]:

$$\Delta\rho\ (\vec{r}) = \rho_{complex}(\vec{r}) - \rho_{substrate}(\vec{r}) - \rho_{biomar\,ker}(\vec{r}), \quad (4)$$

where $\rho_{complex}(\vec{r})$ denotes the charge density of the substrate-biomarker system, $\rho_{substrate}(\vec{r})$ and $\rho_{biomar\,ker}(\vec{r})$ are the charge densities of the substrate and biomarker, respectively.

3.1. Structural Properties

From the perspective of adsorption energy, as recapitulated in **Tables S1** and **S2**, all adsorption configurations exhibit negative values, implying the spontaneous reactions of the above-mentioned biomarkers on the g-C_3N monolayer. In the case of acetaldehyde adsorption, we found that the preferred configuration for the CH_3CHO molecule is the parallel configuration, in which its C-C bond was aligned directly above the carbon atom and O atom of acetaldehyde point to the g-C_3N monolayer (**Figure 5(a)**). The E_{ads} in this system was calculated to be only -319 meV. The adsorption energy results highlight the potential application of the g-C_3N monolayer to serve as a thermopower-based (calorimetric)biosensor [15,45]. Thermopower-based sensors detect an increase in temperature of the sensing material by leveraging the heat released from the reaction. In addition, the adsorption distance was 2.992 Å. This distance value exceeded the chemical interaction limit between the g-C_3N monolayer and the CH_3CHO molecule. Moreover, we observed that the g-C_3N plane and the gas molecule maintain their original structure during the adsorption process, reflecting the preliminary assumption of physical adsorption. The physical adsorption of the gas molecule on the g-C_3N monolayer originates from van der Waals and dipole-dipole interactions. In other words, the charge density distribution along the acetaldehyde molecule is completely asymmetric due to the comparable electronegativity difference between its O and H atoms, inducing bond dipole moment [46]. In response to the dipole moment provided by the acetaldehyde molecule, a dipole moment is induced on the g-C_3N surface. The subsequent subsection provides evidence for this assertion through the charge density redistribution plot. This interaction is also the reason behind the observed surface distortion of 0.078 Å for nitrogen and 0.052 Å for carbon atoms under the gas molecule.

For propane adsorption, it can be seen that the C_3H_8 molecule was preferably adsorbed on the g-C_3N surface in a perpendicular orientation with the middle carbon atom aligned almost above the g-C_3N nitrogen atom (**Figure 5(b)**). The physisorption nature of this system is demonstrated by low adsorption energy (-293 meV) and long adsorption distance (2.701 Å) listed in Table **S2**. Moreover, the adsorption of propane induced a slight change in the bond lengths and angles of the g-C_3N monolayer. A local structural distortion was observed in the g-C_3N below the adsorption area.

The overlapping of the wave function along the z direction, as shown by the color contour in **Figure 6**, signifies the weak (physical) interaction between the considered biomarkers and the sensor surface during the adsorption process. As a consequence, the desorption times (Equation (2)) of acetaldehyde and propane molecules from the g-C_3N surface at room temperature (T = 300 K) under visible light exposure ($\nu = 10^{12}$ s^{-1}) are 235 ns and 222 ns, respectively, implying the instantaneous desorption process.

3.2. Electronic properties

To investigate the influence of biomarkers' adsorption on the electronic properties of the relaxed g-C_3N monolayer, its electronic band structure, total and projected density of states were investigated in the presence of gas molecules. The band structure of the g-C_3N monolayer following acetaldehyde adsorption is depicted in **Figure 7(a)**, indicating a direct band gap, with both the valence band maximum and the conduction band minimum located at the Γ point. The valence and conduction bands lie 0.190 eV below and 0.192 eV above the Fermi energy level, respectively, implying the p-type characteristic. The change of g-C_3N monolayer semiconductor property from n-type into p-type enables its use as a Seebeck effect-type sensor. Furthermore, the energy band gap experienced a significant reduction from 437 meV to 382 meV after interaction with the acetaldehyde molecule. The decline of the energy band gap is associated with the contribution of the adsorbed molecule's density of state near the Fermi level. At the same time, further away from the Fermi level, orbital hybridization occurs between the host material and biomarker, leading to the much denser states. Consequently, the presence of the acetaldehyde molecule can be detected by monitoring the changes in conductivity. As observed in **Figure 7(a)**, adsorption of this biomarker leaves the general shape of the g-C_3N monolayer's DOS intact but enhances the peak intensities due to orbital overlapping, a clear indicator of a strong interaction.

During the adsorption of the acetaldehyde molecule on the g-C_3N monolayer, the adsorbed molecule acquires 0.045 e from the host material, underlying the resistive gas sensing mechanism. This charge transfer establishes a local electric field perpendicular to the g-C_3N monolayer and reduces the bond charge density of the monolayer at the adsorption site. The resultant charge depletion weakens the local bonds, which manifests as an elongation of bond lengths and a reduction of bond angles. The charge-transfer path could be identified from the energy-level diagrams of individual elements, as shown schematically in **Figure 8(a)**. Based on the highest occupied molecular orbital (HOMO) and lowest unoccupied molecular orbital (LUMO) representations, we can find that the HOMO of the isolated acetaldehyde molecule is mainly located 3.244 eV below the g-C_3N conduction band, while its LUMO is located near 1.054 eV above the g-C_3N valence band. Considering the small difference between the valence band of the adsorbent and the LUMO energy of the biomarker molecule, electrons tend to flow along the blue arrow path.

Moreover, the calculation results show that the Fermi energy level of the g-C_3N monolayer shifted downwards. Therefore, its work function value (Equation (3)) increased from 2.899 eV to 2.93 eV after acetaldehyde adsorption, aligned with the direction of charge transfer. The shift in the Fermi level provides an opportunity to identify acetaldehyde in the exhaled breath by comparing the electrical signal.

The charge density redistributions (Equation (4)), due to the presence of the acetaldehyde molecule, are illustrated in **Figure (9)**. According to this figure, electron accumulation (depletion) around the gas molecule (g-C_3N) in the yellow (green) cloud also authenticates the charge transfer direction during the adsorption process. The similarity of the spin-up and spin-down electron redistributions in **Figures 9(a) and (b)**, as well as the equality of the excess spin-up and spin-down electrons in **Figure 9(d)**, is consistent with the non-magnetic nature of the adsorbed system. At the same time, the polarized acetaldehyde molecule induced polarity and thereby an electric dipole moment in the g-C_3N surface, as shown in **Figure 9(c)**, leading to stronger physisorption through dipole-dipole interactions.

Regarding the adsorption of the propane molecule, one can see that the band structure and DOS of the g-C_3N monolayer remained almost unchanged near the Fermi level (**Figure 7(b)**). This is consistent with the small value of the adsorption energy mentioned earlier. Following the propane molecule adsorption, the valence and conduction bands are 0.220 eV below and 0.215

eV above the Fermi energy level, respectively, indicating an n-type semiconducting property. The minor alteration of the g-C_3N monolayer energy band gap correlates with a small change in conductivity. It is noticeable that the achieved response can be improved by making some modifications to this material, which is the subject of our future work. Meanwhile, flat bands exist below the Fermi level around -5 eV, belonging to the C 2p orbitals of propane. These orbitals do not hybridize with the monolayer orbitals and consequently maintain non-dispersive character.

According to the charge transfer analysis findings, in the absence of an external field, the g-C_3N monolayer lost 0.021 e during adsorption, and the propane molecule acted as an electron acceptor. The observed charge transfer value corroborates the interaction energy value. The energy levels of the adsorbent material and the biomarker molecule are portrayed in **Figure 8(b)**. The HOMO and LUMO energy levels of the isolated gas molecule were calculated as -7.691 eV and -0.497 eV, respectively. The proximity of the g-C_3N valence band to the LUMO of propane determines the charge transfer direction from the former to the latter. Based on our results, there was a small change in the work function value (Equation (3)) of the propane/g-C_3N system.

The charge density redistribution plot of the adsorbed system shown in **Figure 10** is similar to the adsorption of acetaldehyde, in which electrons were depleted from the g-C_3N monolayer and accumulated close to the H atoms in the propane molecule, manifesting the electron-withdrawing property of the C_3H_8 molecule. As expected, the small charge transfer in the adsorption process led to weak electron redistribution to the whole system. The spin-distinct charge density plot (**Figure 10(d)**) shows spin-up and spin-down charge accumulation around carbon and nitrogen atoms, respectively.

In order to further explore the potential of the g-C_3N monolayer for the detection of acetaldehyde and propane, the obtained results were compared with some earlier works and summarized in **Tables 1 and 2** [47-57]. Based on the presented data in **Table 1**, the g-C_3N monolayer exhibits better acetaldehyde sensing performance in terms of the amount of charge transfer and the change in energy band gap compared to other compounds. Some sensing materials have higher negative adsorption energy values, prolonging the recovery process and impeding their practical applications. However, it can be found that the propane sensing characteristics of the g-C_3N monolayer are lower than those reported in the literature and need to be improved (**Table 2**).

Previous studies investigated the sensing capability g-C_3N monolayer toward some lung cancer biomarkers and volatile organic compounds [31, 58]. **Figure 11** compares the adsorption energy of those reported in the literature with the adsorption energy of the biomarkers considered in this study. The adsorption energy values lie around -90 meV to -250 meV, indicating no chemical bonding and weak physisorption. The moderate adsorption strength and apparent changes in the electronic properties of the pristine g-C_3N monolayer in the adsorption of acetaldehyde and propane make it a promising prospect for a highly sensitive and reusable gas sensor.

3.3. Effect of an external electric field

To evaluate the adsorption properties of the adsorbent surface toward each biomarker in the presence of a vertical electric field, their most stable adsorption configurations were considered. Calculated adsorption energy and adsorption distance under various strengths of external electric field are revealed in **Figure 12**. A close examination of the relaxed geometries shows that the atomic arrangements of the adsorbed systems were little affected by the external electric field. The bond lengths and bond angles experienced small changes compared to their pristine counterpart. However, the adsorption energy of the biomarker molecules on the g-C_3N monolayer was directly governed by the applied electric field. In other words, the external electric field promoted the ability of the g-C_3N monolayer to adsorb gas molecules. Notably, the desorption of biomarkers may be more difficult under a higher external electric field. The minimum interaction distance between the gas molecules and the substrate shows a downward trend with increasing electric field intensity, which contributes to the stronger interaction. The observations indicate that the adsorption distance of the acetaldehyde molecule was more sensitive to the external electric field. Moreover, the interaction distance was greater than the sum of the covalent radius of the related atoms, implying non-covalent interactions.

The reason for the drastic enhancement in adsorption energy is connected with the excess charge transfer from the g-C_3N monolayer to the gas molecule. The net charge transfer versus electric field strength is shown in **Figure 12(c)**. Increasing the charge transfer for a given electric field was greater for the g-C_3N substrate with acetaldehyde than for propane. The largest value of the electrons captured by this biomarker is under the electrical field of 0.22 V/Å. Applying an external electric field yielded an additional electron flow from the former to the latter. The

charge accumulation near the gas molecules and a charge depletion near the g-C_3N monolayer reinforced the built-in electric field between them. As the charge transfer increases, the repulsive force between biomarker and adsorbent magnifies, and the built-in electric field is strengthened, which can be better illustrated by the charge density redistribution plot. In order to make sense of the compound charge depletion (or accumulation), we plot the charge density redistribution for adsorbed compounds in response to the electric fields of 0.03 V/Å and 0.19 V/Å in **Figure 13**.

In terms of electronic properties, the application of an electric field caused the conduction band states (valence band states) of the g-C_3N monolayer to shift upwards(downward), resulting in the gradual widening of the energy band gap. Moreover, the progressive increment of the electric field strength led to a shift in the Fermi energy level towards lower energy states (valence band). When the electric field exceeded a certain value, the Fermi level crossed the valence band, rendering the structure a metallic character. Metallic behavior persisted with further increases in electric field strength. The energy band structure of the g-C_3N monolayer and the adsorbed systems in the presence of different electric field strengths are depicted in **Figures S5** and **Figure 14**, respectively. The computed energy band gaps are shown in **Figure 15(a)**. The g-C_3N monolayer was converted into a metallic system by the adsorption of acetaldehyde and propane in the presence of a lower external electric field. The applied electric field acted as a p-type (hole) doping of the semiconductor. Chemical p-type doping introduces acceptor atoms that shift the Fermi level toward the valence band. When a positive electric field is applied, the valence band is brought close to the Fermi level, replicating the key electronic characteristic of a p-type semiconductor. The downward shift in the Fermi energy level (degree of hole doping) increased with the electric field, and a smaller energy band gap was achieved. Alteration in the band gap in the presence of target gas molecules triggers measurable changes in the conductivity of gas-sensitive material, allowing the use of the g-C_3N monolayer as a resistance-based biosensor.

Next, we considered the work function variation due to the external electric fields to study the theoretical viability of the work function-based lung cancer biosensor (**Figure 15(b)**). Since the Fermi energy level was shifted downwards by increasing the electric field, the related work function increased significantly. This finding supports its application as an effective lung cancer biomarker detector based on work function measurements with the help of an extra electric field.

4. Conclusion

Inspired by the importance of early diagnosis of lung cancer, which is responsible for most cancer-related deaths worldwide, we performed first-principles calculations using DFT to examine the optimized geometries, electronic and sensing properties of the pristine g-C_3N monolayer toward two expiratory biomarkers of lung cancer, namely propane and acetaldehyde, in the absence and presence of an external electric field. The adsorption energy values and adsorption distances signify the physical and exothermic interactions. The moderate physisorption interaction triggered between lung cancer biomarkers and pristine g-C_3N monolayer due to the van der Waals interaction, yielded a fast desorption process under visible light at room temperature. The Löwdin charge analysis indicated that g-C_3N behaves as an electron donor for adsorbed biomarkers in accordance with the charge density difference. Furthermore, the adsorption of acetaldehyde can cause a reduction in the energy band gap of g-C_3N, which in turn increases electrical conductivity and consequently the sensor response. Under an external electric field, there was an extra charge transferred from the pristine g-C_3N monolayer to the adsorbed biomarkers, which was reflected in the adsorption energy. Furthermore, the sensing material energy band gap experienced steep variations in the presence of characteristic VOCs of exhaled breath above an electric field of 0.11 V/Å. Given that the g-C_3N monolayer's work function increased in the presence of biomarkers, the work function-based sensor can be designed. Based on these findings, a pristine g-C_3N monolayer is amenable to preliminary diagnosis of lung cancer in thermopower-based, Seebeck-effect-based, resistance-based, or work function-based sensors.

Declaration of competing interest

The authors declare that they have no known competing financial interests or personal relationships that could have appeared to influence the work reported in this paper.

Funding

This research received no specific grant from any funding agency in the public, commercial, or not-for-profit sectors.

Data availability

The raw data supporting the conclusion of this article will be made available from the corresponding author, without undue reservation.

Acknowledgments

The authors thank the support of this work by the Research Council of Shiraz University. The authors gratefully acknowledge the Sheikh Bahaei National High Performance Computing Center (SBNHPCC) for providing computing facilities and time. SBNHPCC is supported by scientific and technological department of presidental office and Isfahan University of Technology (IUT).

References

[1] A. Leiter, R. R.Veluswamy, J. P. Wisnivesky, The global burden of lung cancer: current status and future trends, Nature Rev. Clin. Oncol. 20 (2023) 624-639.

[2] F. Bray, M. Laversanne, H. Sung, J. Ferlay, R. L. Siegel, I. Soerjomataram, A. Jemal, Global cancer statistics 2022: GLOBOCAN estimates of incidence and mortality worldwide for 36 cancers in 185 countries, CA: Cancer J. Clin. 74 (2024) 229-263.

[3] J. A. Barta, C. A. Powell, J. P. Wisnivesky, Global epidemiology of lung cancer, Ann. Glob. Health 85 (2019) 8.

[4] J. C. Laguna, M. García-Pardo, J. Alessi, C. Barrios, N. Singh, H. O. Al-Shamsi, H. Loong, M. Ferriol, G. Recondo, L. Mezquita, Geographic differences in lung cancer: focus on carcinogens, genetic predisposition, and molecular epidemiology, Ther. Adv. Med. Oncol. 16 (2024) 17588359241231260.

[5] A. Pulumati, A. Pulumati, B. S. Dwarakanath, A. Verma, R. V. L. Papineni, Technological advancements in cancer diagnostics: Improvements and limitations, Cancer Rep. 6 (2023) 1–17.

[6] S. Connal, J. M. Cameron, A. Sala, P. M. Brennan, D. S. Palmer, J. D. Palmer, H. Perlow, M. J. Baker, Liquid biopsies: the future of cancer early detection, J. Transl. Med. 21 (2023) 118.

[7] H. Khan, M. R. Shah, J. Barek, M. I. Malik, Cancer biomarkers and their biosensors: A comprehensive review, TrAC - Trends Anal. Chem. 158 (2023) 116813.

[8] J. Zhou, Z.A Huang, U. Kumar, D. D.Y. Chen, Review of recent developments in determining volatile organic compounds in exhaled breath as biomarkers for lung cancer diagnosis, Anal. Chim. Acta 996 (2017) 1-9.

[9] Q. Hua, Z. Yanzhe, L. Hu, Detection of volatile organic compounds in exhaled breath to screen lung cancer, A systematic review, Future Oncol. 14 (2018) 1647-1662.

[10] V. Vassilenko, P. C. Moura, M. Raposo, Diagnosis of carcinogenic pathologies through breath biomarkers: Present and future trends, Biomed. 11 (2023) 3029.

[11] D. Smith, T. Wang, J. Sulé-Suso, P. Španěl, A. E. Haj, Quantification of acetaldehyde released by lung cancer cells in vitro using selected ion flow tube mass spectrometry, Rapid Commun. Mass Spectrum. 17 (2003) 845-850.

[12] H. C. Chuang, S. W. Tsai, R. H. Shie, Y. C. Lu, S. R. Song, S. H. Huang, H. Y. Peng, H. Y. Yang, A novel lung alveolar cell model for exploring volatile biomarkers of particle-induced lung injury, Sci. Rep. 10 (2020) 15700.

[13] F. Gouzerh, J. M. Bessière, B. Ujvari, F. Thomas, A. M. Dujon, L. Dormont, Odors and cancer: Current status and future directions, Biochim. Biophys. Acta (BBA)-Rev. Cancer 1877(2022) 188644.

[14] B. Ding, Y. Song, S. Liu, C. Peng, Y. Zhang, Mechanisms underlying the changes in acetaldehyde dehydrogenase 1 in cholangiocarcinoma, J.Cancer, 14(17) (2023) 3203.

[15] S. Nikmanesh, R. Safaiee, M. H. Sheikhi, A novel high-performance methane sensor based on Ti-Decorated 2D γ-graphyne: A dispersion-corrected DFT insight, Mater. Chem. Phys, (2021) 123808.

[16] J. Z. Hassan, A. Raza, Z. U. D. Babar, U. Qumar, N. T. Kaner, A. Cassinese, 2D material-based sensing devices: an update, J. Mater. Chem. A 11(2023) 60166063.

[17] S. Li, L. Zhang, Accurate first-principles simulation for the response of 2D chemiresistive gas sensors, npj Comput. Mater. 10.1 (2024) 138.

[18] R. Rahimi, M. Solimannejad, Z. Ehsanfar, A computational exploration of promising sensing of lung cancer biomarkers using a novel polyaramid nanosheet, J. Mol. Liq. (2025) 128612.

[19] R. Rahimi, M. Solimannejad, A. Chaudhari, Toxic volatile organic compounds sensing by Al_2C monolayer: a first-principles outlook, J. Hazard. Mater. 403(2021) 123600.

[20] R. Rahimi, M. Solimannejad, Exploring the adsorption behavior of O-containing VOCs in human breath on a B_2N monolayer using DFT simulations, Phys. Chem. Chem. Phys. 26(39) (2024) 25567-25580.

[21] R. Rahimi, M. Solimannejad, $B_3C_2N_3$ monolayer as a potential biosensor for the sensitive and selective detection of liver cancer biomarkers: A DFT study, Mater. Sci. Semicond. Process. 186 (2025) 109025.

[22] J. Mahmood, E. K. Lee, M. Jung, D. Shin, H. J. Choi, J. M. Seo, S.M. Jung, D. Kim, F. Li, M. S. Lah, N. Park, H. J. Shin, J. H. Oh, J. B. Baek, Two-dimensional polyaniline (C_3N) from carbonized organic single crystals in solid state, Proc. Natl. Acad. Sci. U. S. A.113 (2016) 7414–7419.

[23] Y. H. Yin, C. Lu, The non-covalent interaction between C_3N and H_2. Comput. Theor. Chem. 1242 (2024) 114951.

[24] L. Xie, L. Yang, W. Ge, X. Wang, J. Jiang, Bandgap tuning of C_3N monolayer: A first-principles study, Chem. Phys. 520 (2019) 40–46.

[25] A. Bafekry, C. Stampfl, S. F. Shayesteh, F. M. Peeters, Exploiting the novel electronic and magnetic structure of C_3N via functionalization and conformation, Adv. Electron. Mater. 5 (2019) 1–17.

[26] O. Faye, T. Hussain, A. Karton, J. Szpunar, Tailoring the capability of carbon nitride (C_3N) nanosheets toward hydrogen storage upon light transition metal decoration, Nanotechnol. 30(7) (2018) 075404.

[27] X. Wang, Q. Li, H. Wang, Y. Gao, J. Hou, J. Shao, Anisotropic carrier mobility in single-and bi-layer C_3N sheets, Phys. B: Condens. Matter. 537 (2018) 314-319.

[28] Z. Chen, H. Wang, Z. Li, First-principles study of two dimensional C_3N and its derivatives. RSC adv.10(55) (2020) 33469-33474.

[29] L. Tan, C. Nie, Z. Ao, H. Sun, T. An, S. Wang, Novel two-dimensional crystalline carbon nitrides beyond g C_3N_4: Structure and applications, J. Mater. Chem. A 9 (2021) 17-33.

[30] O. Faye, U. Eduok, J. A. Szpunar, A. C. Beye, Two-dimensional carbon nitride (C_3N) nanosheets as promising materials for H_2S and NH_3 elimination: A computational approach, Phys. E: Low-Dimensional Syst. Nanostruct. 117 (2020) 113794.

[31] S. Agrawal, G. Kaushal, A. Srivastava, Electron transport in C_3N monolayer: DFT analysis of volatile organic compound sensing, Chem. Phys. Lett. 762 (2021) 138121.

[32] H. Cui, C. Yan, P. Jia, W. Cao, Adsorption and sensing behaviors of SF_6 decomposed species on Ni-doped C_3N monolayer: A first-principles study, Appl. Surf. Sci. 512 (2020) 145759.

[33] D. Ma, J. Zhang, X. Li, C. He, Z. Lu, Z. Lu, Z. Yang, Y. Wang, C_3N monolayers as promising candidates for NO_2 sensors, Sens. Actuators B: Chem. 266 (2018) 664–673.

[34] J. Zhao, W. Li, S. A. Aslanzadeh, A DFT study on the adsorption of DNA nucleobases on the C_3N nanotubes as a sequencer, J. Mol. Model 27(2021) 57.

[35] P. Giannozzi, S. Baroni, N. Bonini, M. Calandra, R. Car, C. Cavazzoni, D. Ceresoli et al. QUANTUM ESPRESSO: a modular and open-source software project for quantum simulations of materials, J. Phys. Condens. Matter 21 (2009) 395502.

[36] J. P. Perdew, K. Burke, M. Ernzerhof, Generalized gradient approximation made simple, Phys. Rev. Lett. 77 (1996) 3865.

[37] S. Grimme, Semiempirical GGA-type density functional constructed with a long-range dispersion correction, J. Comput. Chem. 27 (2006) 1787-1799.

[38] T. Bucko, J. Hafner, S. Lebègue, J. G. Angyán, Improved description of the structure of molecular and layered crystals: ab initio DFT calculations with van der Waals corrections, J. Phys. Chem. A 114 (2010) 11814-11824.

[39] T. Brumme, M. Calandra, F. Mauri, Electrochemical doping of few-layer ZrNCl from first principles: Electronic and structural properties in field-effect configuration, Phys. Rev. B 89 (2014) 245406.

[40] B. I. Weintrub, Y. L. Hsieh, S. Kovalchuk, J. N. Kirchhof, K. Greben, K. I. Bolotin, Generating intense electric fields in 2D materials by dual ionic gating, Nat. Commun. 13(1) (2022) 6601.

[41] L. Zhang, Y. Liu, M. Wu, G. Gao, Electric-field- and stacking-tuned antiferromagnetic FeClF bilayer: The coexistence of bipolar magnetic semiconductor and anomalous valley hall effect, Adv. Funct. Mater. 35(17) (2025) 2417857.

[42] F. D. Murnaghan, The compressibility of media under extreme pressures, Proc. Natl. Acad. Sci. 30(9) (1944) 244-247.

[43] S. Nikmanesh, R. Safaiee, M. H. Sheikhi, Enhanced methane-sensing performances of Pd (monomer or dimer) decorated or doped γ-Graphyne: A DFT insight, Surf. Interfaces 29 (2022) 101658.

[44] Sh. Nasresfahani, R. Safaiee, M. H. Sheikhi, Application feasibility of palladium-decorated reduced graphene oxide as a CH_4 gas nano-sensor from the perspective of the van der Waals corrected DFT computations, Phys. E: Low-dimens. Syst. Nanostruct. 134 (2021) 114866.

[45] G. Korotcenkov, Catalysts used in calorimetric (Combustion-Type) gas sensors, Handbook of gas sensor materials, Springer, New York, NY (2013).

[46] F. Delbecq, F. Vigné, Acetaldehyde on Pt (111) and Pt/Sn (111): a DFT study of the adsorption structures and of the vibrational spectra, J. Phys. Chem. B 109(21) (2005) 10797-10806.

[47] X. Q. Lin, Z. H. Han, X. Zhang, J. X. Yang, Y. G. Yao, Boron-doped ZrS_2 monolayer as a promising gas sensing material for the detection of volatile organic compounds: A DFT study. Phys. Chem. Chem. Phys. 2025,27 (2025) 22809-22819.

[48] W. Xiao, Z. Wang, Y. Gui, Adsorption properties of metal atom (Co, V, W, Zr)-modified $MoTe_2$ for CO, CH_3CHO, and C_6H_6 gases: A DFT study, Molecules 29 (2024) 5086.

[49] H. Zhang, L. Xu, Y. Gui, Adsorption and gas-sensing properties of the metal (Co and Zr) modified $MoSe_2$ monolayer upon air pollution gases (C_6H_6, CH_3CHO and CO), Mater. Sci. Semicond. Process. 200(2025) 109920.

[50] K. Seidali Javanmardi, Z. Karami Horastani, The potential application of SiC_2 monolayer in sensing acetaldehyde, acetone, and ammonia gases as health screening biomarkers and air pollutants: a DFT study, Eur. Phys. J. Plus 139(7) (2024) 567.

[51] R. Rahimi, M. Solimannejad, Sensing response of pentagonal B_2C nanosheet towards VOCs: a study combining DFT and molecular dynamics simulations, Chem. Phys. 574(2023) 112042.

[52] R. M. Ahangar, D. Farmanzadeh, O-doping effects on the adsorption and detection of acetaldehyde and ethylene oxide on phosphorene monolayer: A DFT investigation, Chem. Phys. Lett. 813(2023) 140315.

[53] B. Liu, W. Zhao, Q. Jiang, Z. Ao, T. An, Enhanced adsorption mechanism of carbonyl-containing volatile organic compounds on Al-decorated porous graphene monolayer: a density functional theory calculation study, Sustain. Mater. Technol. 21(2019) 00103.

[54] I. Maity, S. Bhanja, First principle based computations to evaluate propane and butane detection capabilities of gold doped graphene based gas sensor devices, In EPJ Web of Conferences (2025) (Vol. 325, p. 01006) EDP Sciences.

[55] R. S. Singh, Sulfur-doped silicon carbide nanotube as a sensor for detecting liquefied petroleum gas at room temperature, Diam. Relat. Mater.124 (2022) 108932.

[56] R. Bhuvaneswari, V. Nagarajan, R. Chandiramouli, Physisorption of propane and butane vapors on novel Kagome antimonene sheets–a first-principles perception, Chem. Phys. Lett. 754(2020) 137693.

[57] V. Nagarajan, R. Chandiramouli, Sensing ability of liquefied petroleum gas by epsilon phosphorene nanosheets-a DFT investigation, J. Mater. NanoSci. 9(2) (2022) 132-137.

[58] K. Ma, Y. Wang, Y. Zheng, J. Xiao, L. Xu, X. Dai, Z. Wang, Adsorption mechanism and optical behaviors of typical volatile organic compounds on pristine and Cu/Ni-Modified C_3N monolayer: A first-principles study, Adv. Theory Simul. 6(1) (2023) 2200611.

Table 1. Comparison of the acetaldehyde sensing performances of g-C_3N monolayer with those of some earlier 2D materials.

Sensing material	E_{ads} (eV)	Adsorption distance (Å)	τ(s)	ΔE_g (eV)	Q (|e|)	Ref.
Pristine ZrS_2	-0.241	2.59	1.1×10^{-8}	~ 0	0.01	[47]
B–ZrS_2	-0.775	1.495	9.810	0.833	0.245	
Co-MoTe2	-0.392	3.288	3.74×10^{-6}	0.008	0.084	[48]
V-$MoTe_2$	-0.405	3.151	6.18×10^{-6}	0.016	0.082	
W-$MoTe_2$	-0.386	3.383	2.97×10^{-6}	0.002	0.079	
Zr-$MoTe_2$	-0.439	3.512	2.30×10^{-5}	0.001	0.063	
MoSe2	-1.314	3.113	2.97×10^{12}	0.005	0.063	[49]
Co-MoSe2	-1.454	1.867	2.4×10^{12}	0.075	0.105	
Zr-$MoSe_2$	-3.029	2.218	6.18×10^{38}	0.142	0.316	
g-SiC2	-0.310	2.45	1.58×10^{-7}	0.011	0.076	[50]
Penta-B_2C nanosheet	-1.06	-	5.94×10^{5}	0.56	0.257	[51]
Black Phosphorus	-0.320	2.930	2.32×10^{-7}	0.003	0.03	[52]
O-doped BP	-0.740	2.90	2.561	0.055	0.03	
Al-graphene	-3.183	-	2.36×10^{41}	-	-0.208	[53]
g-C_3N monolayer	**-0.319**	**2.992**	**2.35**$\times10^{-7}$	**0.055**	**0.045**	**Present work**

Table 2. Comparison of the propane sensing performance of g-C_3N monolayer with those of some earlier nanomaterials.

Sensing material	**E_{ads} (eV)**	**Adsorption distance (Å)**	**τ(s)**	**ΔE_g (eV)**	**Q (|e|)**	**Ref.**
Au doped graphene	-1.074	2.473	-	~ 0 0.833	0.01 0.245	[54]
Si-CNT S-doped Si-CNT	-0.441 -3.144	- 3.071	2.48×10^{-5} 5.24×10^{40}	0.049 0.310	- -	[55]
Sb nanosheet	-1.079	-	1.22×10^{6}	-	0.174	[56]
Epsilon phosphorene nanosheets	-0.732	-	1.881	-	0.096	[57]
g-C_3N monolayer	**-0.293**	**2.701**	**2.22×10^{-7}**	**0.002**	**0.021**	**Present work**

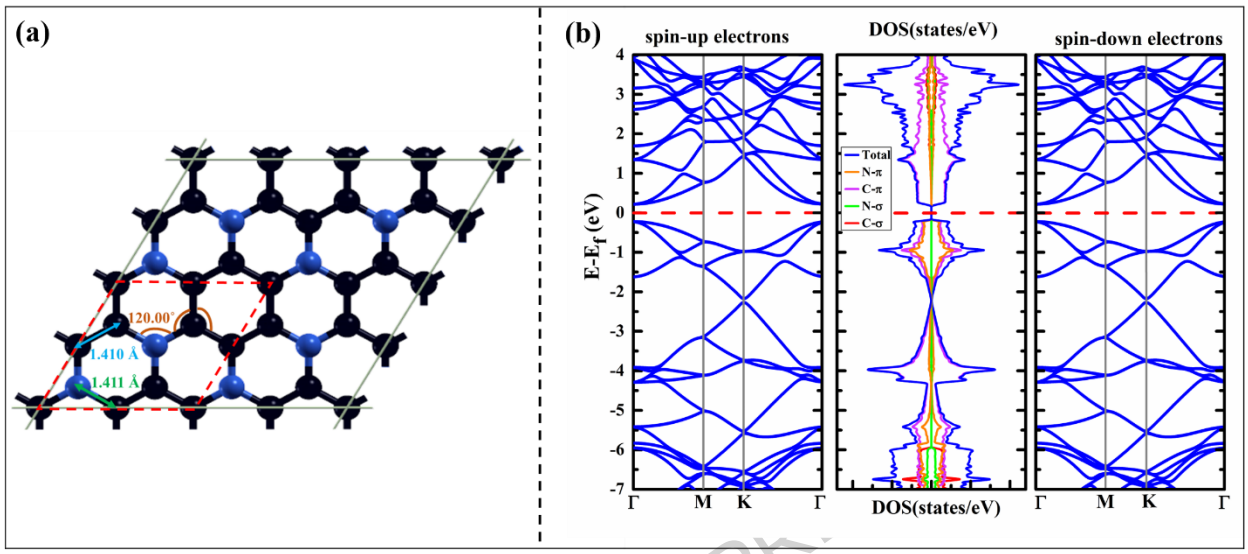

Figure 1. (a) The optimized structure of the pristine g-C_3N monolayer. The carbon and nitrogen atoms were identified by black and dark blue spheres, respectively. (b) Electronic band structure, total density of states, and projected density of states of the relaxed g-C_3N monolayer.

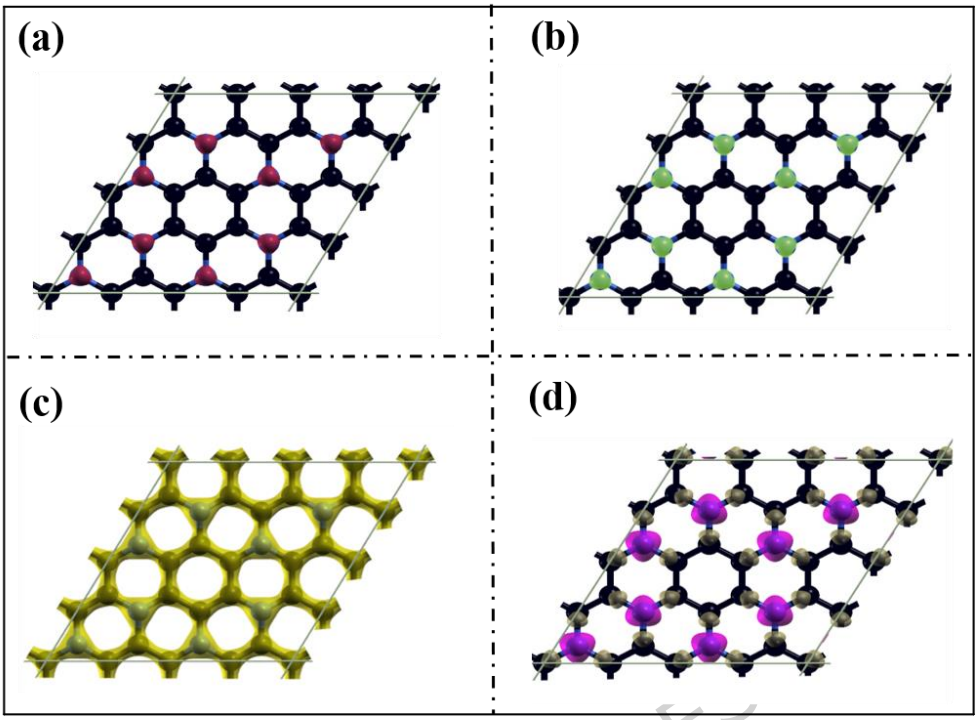

Figure 2. Charge density distribution of the g-C_3N monolayer (a) spin-down, (b) spin-up, (c) total, (d) spin-distinct charge density. The isovalues used in constructing isosurfaces are taken to be 2.15×10^{-1} e e/Bohr^3, for parts (a) to (c), while for the spin-distinct charge density (part (d)), this value is 8×10^{-6} e/Bohr^3.

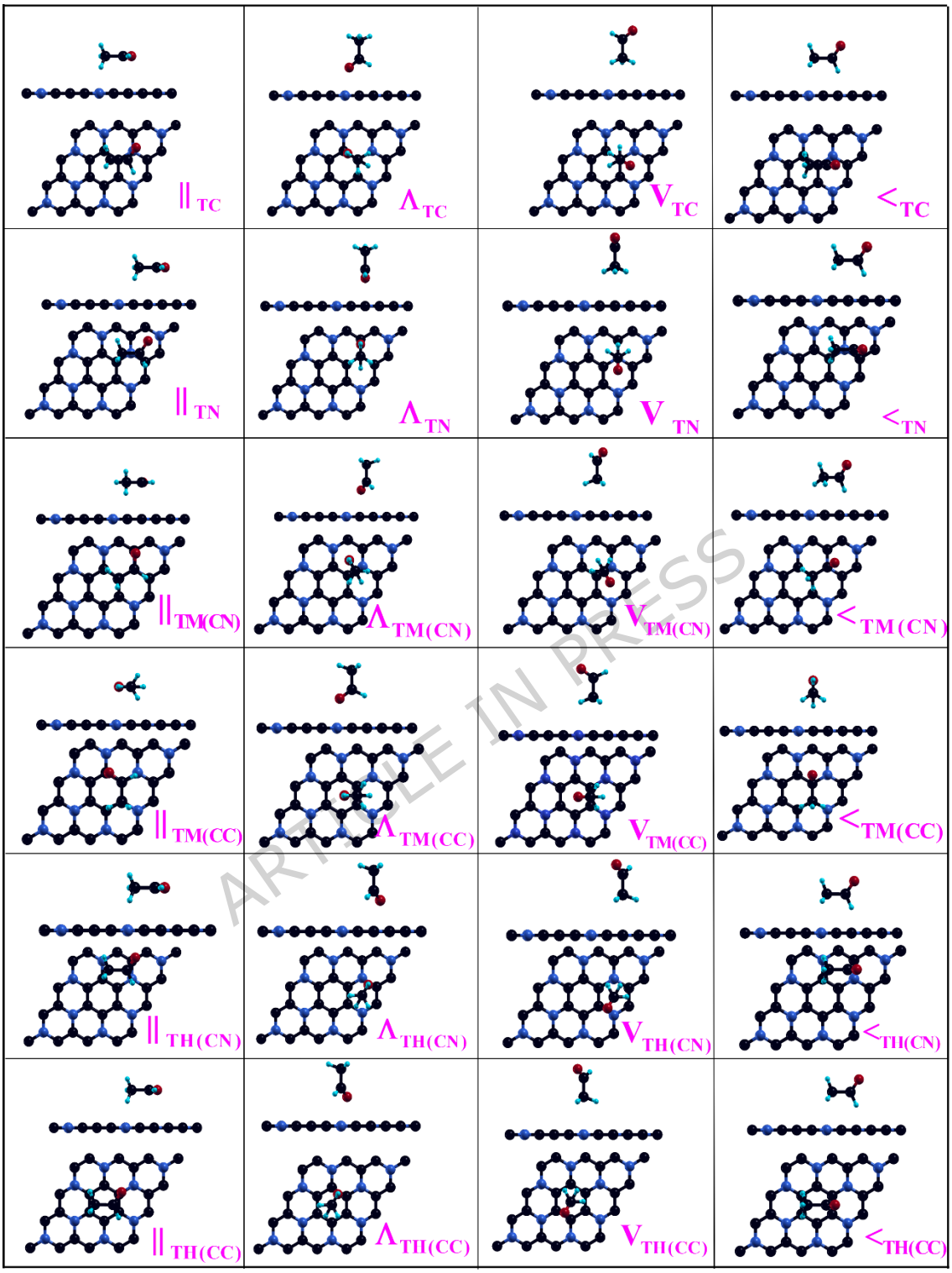

Figure 3. The side and top views of all possible adsorption configurations of acetaldehyde on the g-C_3N substrate. The oxygen (hydrogen) atom was marked by a red (cyan) sphere.

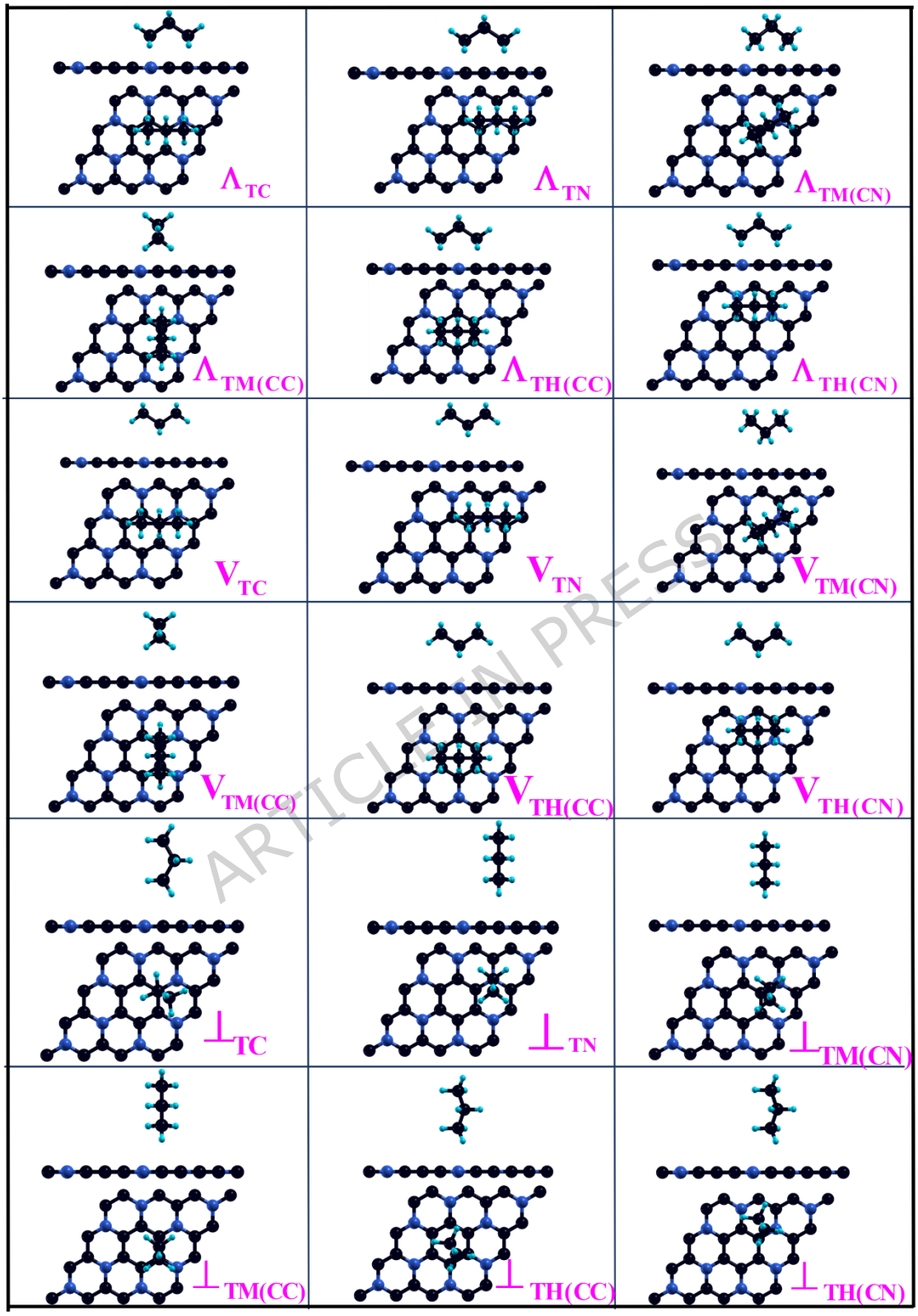

Figure 4. The side and top views of all possible adsorption configurations of propane on the g-C_3N substrate.

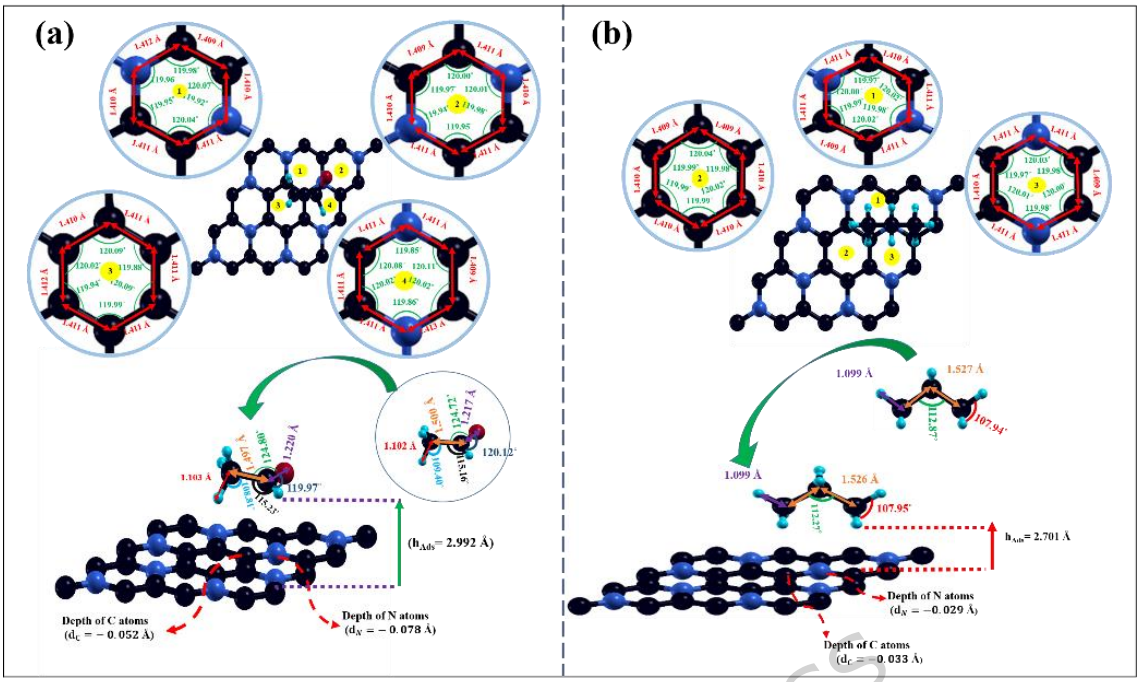

Figure 5. The top and side views of the minimum energy configuration for (a) acetaldehyde, (b) propane on the g-C_3N monolayer.

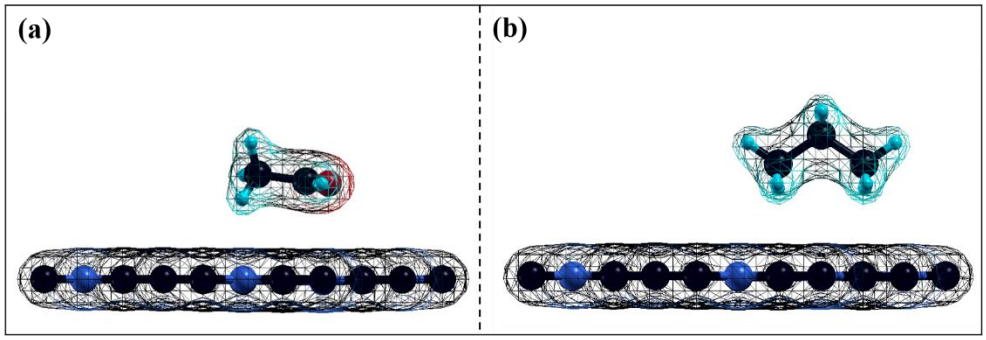

Figure 6. The wave function overlap of the (a) acetaldehyde, (b) propane on the g-C_3N monolayer.

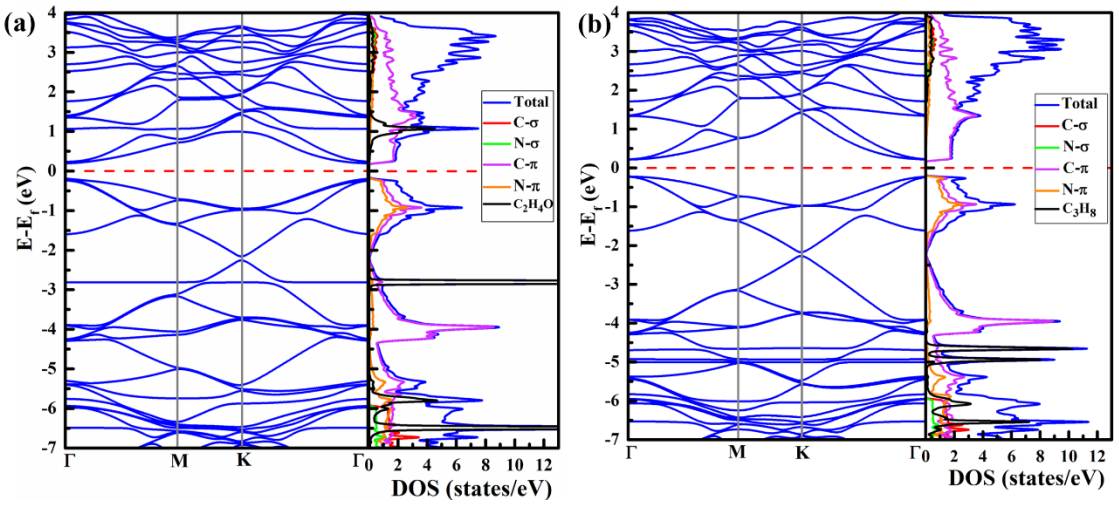

Figure 7. Electronic band structure, total density of states, and projected density of states of the g-C_3N monolayer after adsorption of (a) acetaldehyde, (b) propane. The Fermi energy is set at zero.

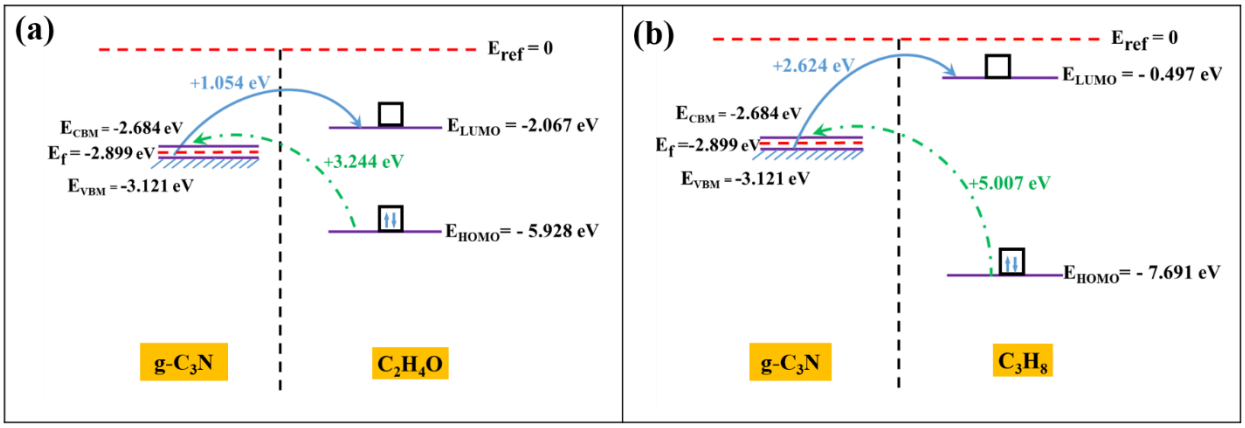

Figure 8. Qualitative energy-level diagrams for g-C_3N monolayer and (a) isolated acetaldehyde molecule, (b) isolated propane molecule.

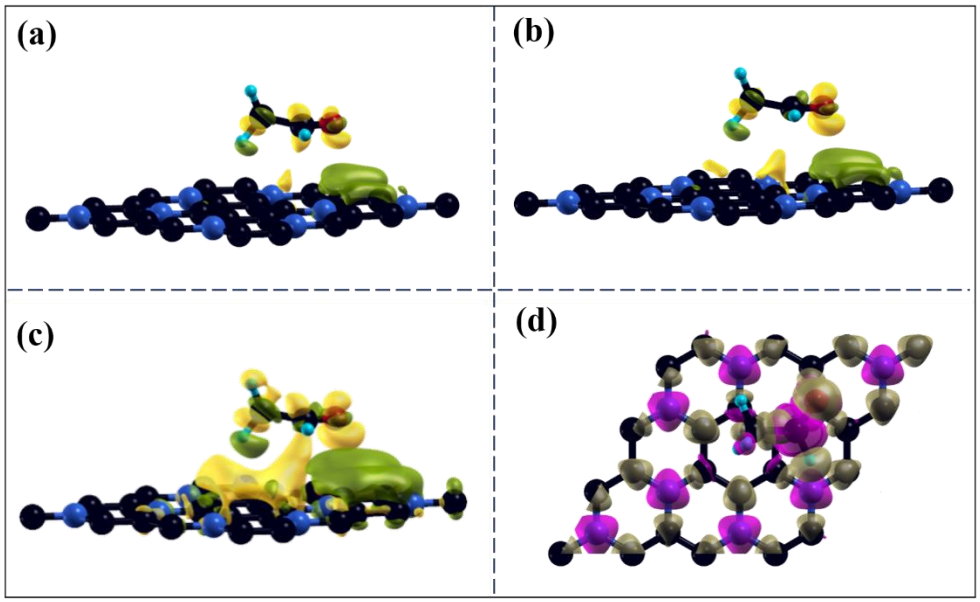

Figure 9. Charge density redistribution of g-C_3N monolayer after acetaldehyde adsorption (a) spin-down, (b) spin-up, (c) total, (d) spin-distinct charge density. The isovalues used in constructing isosurfaces are taken to be 2.6×10^{-4} e/Bohr^3, for parts (a) to (c), while for the spin-distinct charge density (part (d)), this value is 9×10^{-6} e/Bohr^3.

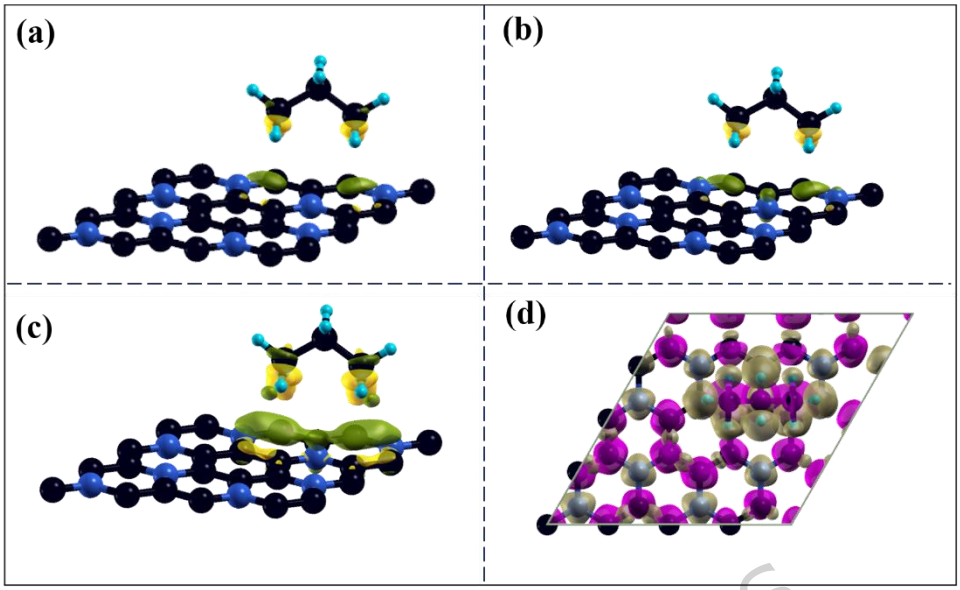

Figure 10. Charge density redistribution of g-C_3N monolayer after propane adsorption (a) spin-down, (b) spin-up, (c) total, (d) spin-distinct charge density. The isovalues used in constructing isosurfaces are taken to be 1.6×10^{-4} e/Bohr^3, for parts (a) to (c), while for the spin-distinct charge density (part (d)), this value is 6×10^{-6} e/Bohr^3.

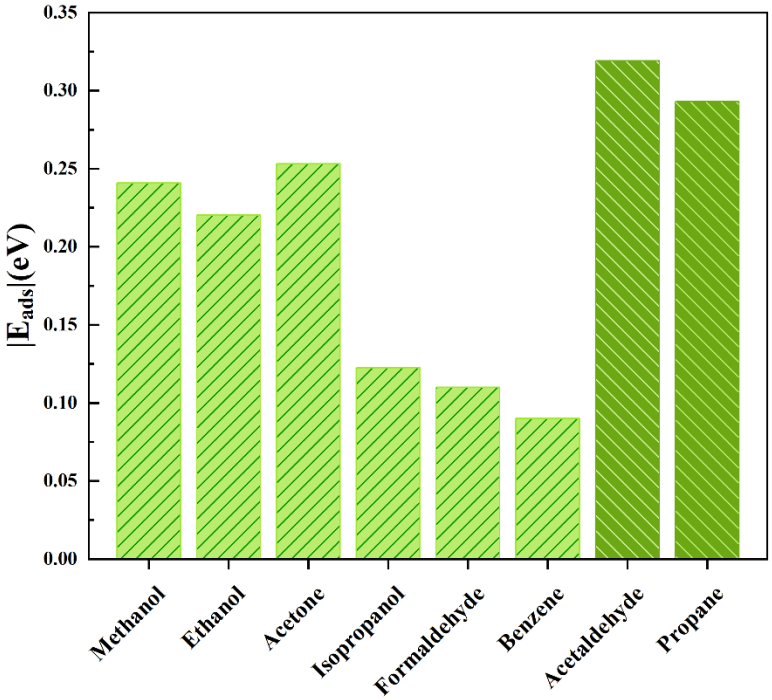

Figure 11. Comparison of the adsorption energies of the different analytes on g-C_3N monolayer.

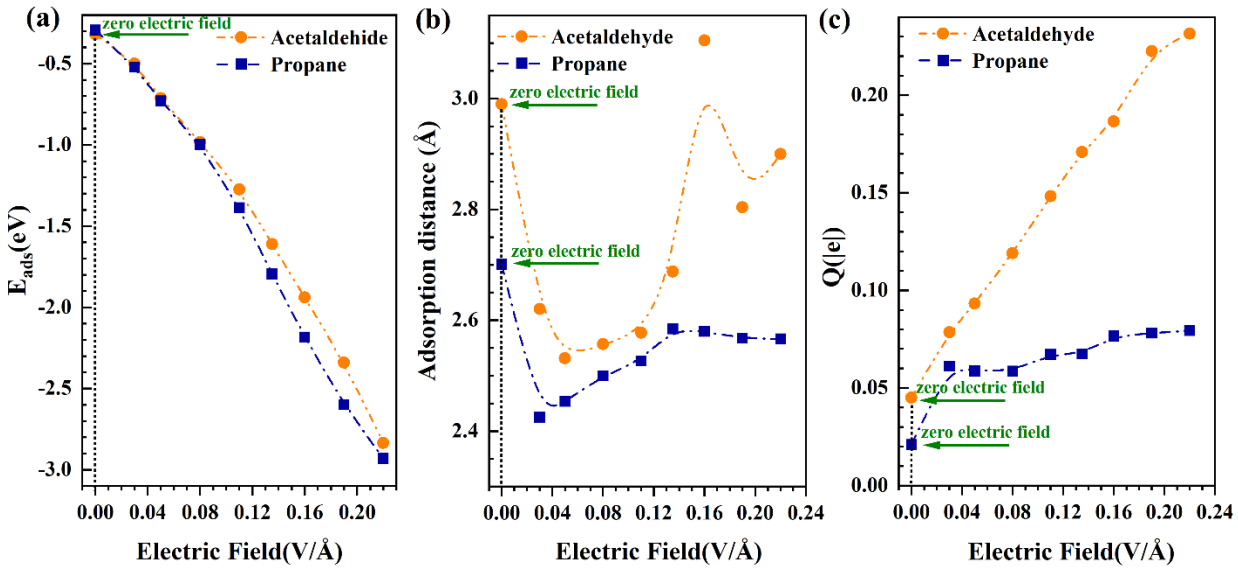

Figure 12. (a) Adsorption energies, (b) adsorption distance, and (c) the net charge transfer of both biomarkers with respect to the applied electric field.

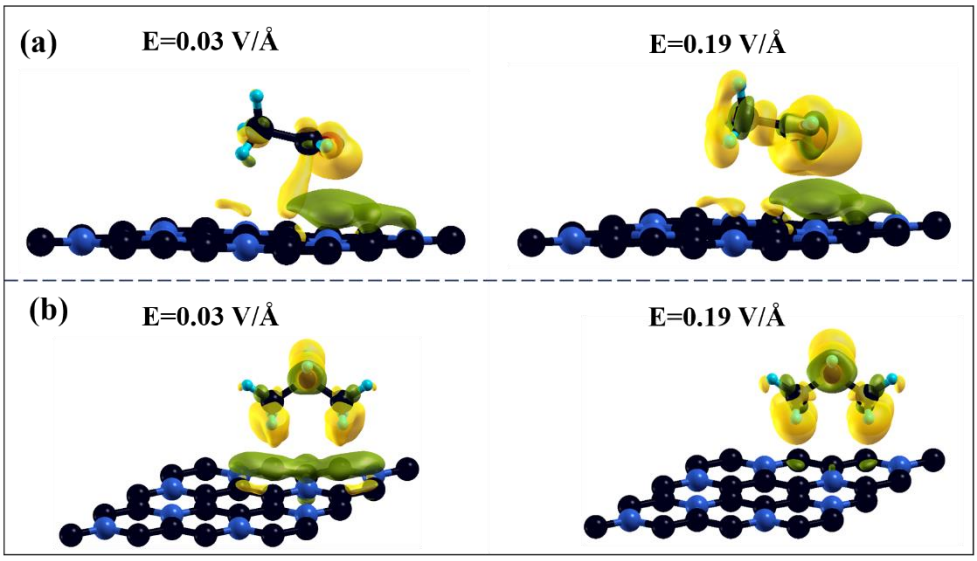

Figure 13. The total charge density redistribution of acetaldehyde and propane adsorbed on the g-C_3N monolayer in response to the electric fields of 0.03 V/Å and 0.19 V/Å. The isosurface value is taken to be 5×10^{-4} e/Bohr^3 for part (a), while for part (b), this value is 1.5×10^{-3} e/Bohr^3 for an electric field of 0.03 V/Å and 5×10^{-4} e/Bohr^3 for the electric field of 0.19 V/Å.

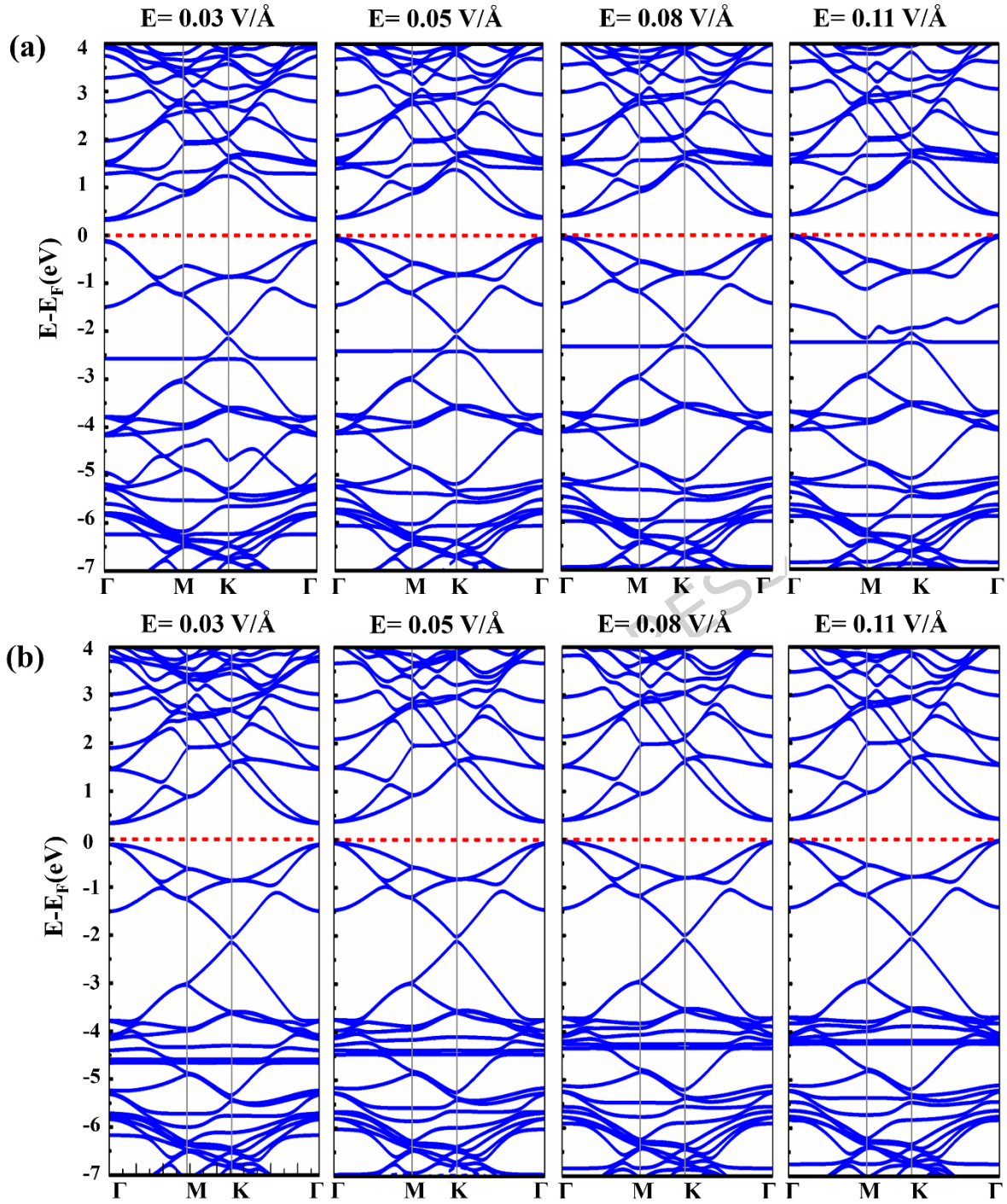

Figure 14. The energy band structure of (a) acetaldehyde, (b) propane adsorbed on the g-C_3N monolayer in the presence of different electric field strengths.

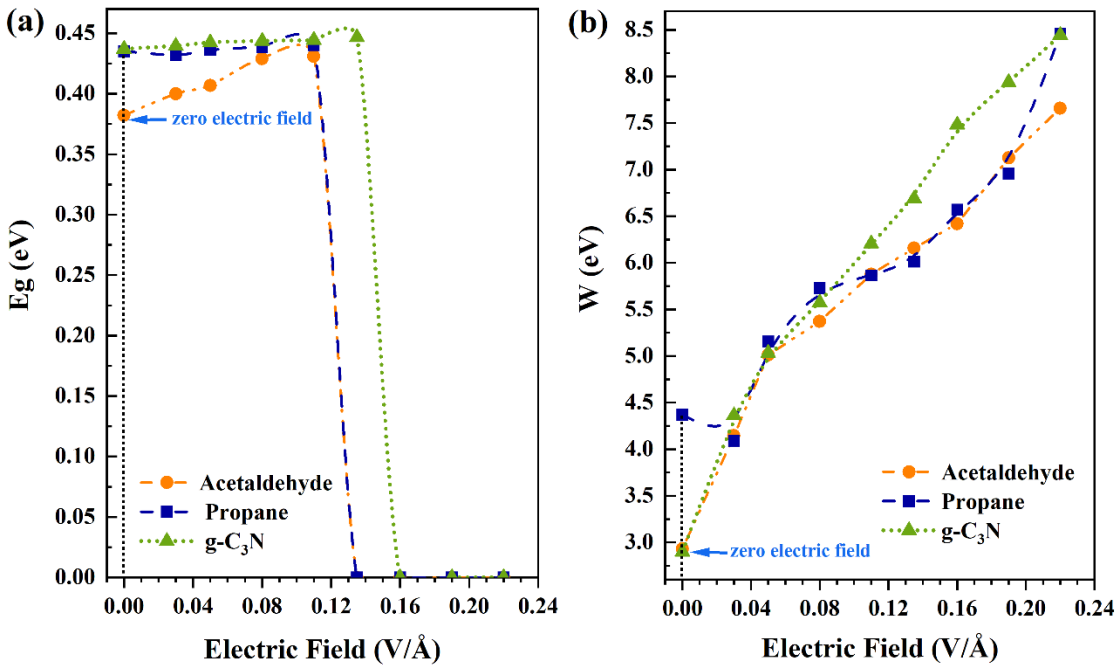

Figure 15. (a) The energy band gap and (b) the work function variations of both biomarkers with respect to the applied electric field.